

# Ultrafast Femtosecond Laser Maskless Patterning for Multitype Microsupercapacitors

**Yongjiu Yuan**

Beijing Institute of Technology <https://orcid.org/0000-0003-0473-1225>

**Lan Jiang**

Beijing Institute of Technology <https://orcid.org/0000-0003-0488-1987>

**Xin Li** (✉ [lixin02@bit.edu.cn](mailto:lixin02@bit.edu.cn))

Beijing Institute of Technology

**Misheng Liang**

Beijing Information Science and Technology University

**Chenyang Xu**

Beijing Institute of Technology

**Le Ma**

Beijing Institute of Technology

**Junrui Wu**

Beijing Institute of Technology

**Junqi Huang**

Beijing Institute of Technology

**Yang Zhao**

Beijing Institute of Technology <https://orcid.org/0000-0002-8187-9963>

**Liangti Qu**

Tsinghua University

---

## Article

### Keywords:

**Posted Date:** February 1st, 2022

**DOI:** <https://doi.org/10.21203/rs.3.rs-1294802/v1>

**License:** © ⓘ This work is licensed under a Creative Commons Attribution 4.0 International License.

[Read Full License](#)

---

# Abstract

Downsizing electrode architectures provides great potential for the fabrication of microscale energy storage devices. With their extended voltage window and high energy density, asymmetric microsupercapacitors (MSCs) play an essential role in various applications. However, the efficient manufacturing of asymmetric MSCs remains challenging. Herein, maskless lithography-based ultrafast fabrication of multitype micron-sized planar MSCs in one step through temporally and spatially shaped femtosecond laser is presented. MSCs are only  $10 \times 10 \mu\text{m}^2$  in size and have a minimum line width of 200 nm. MXene and 1T-MoS<sub>2</sub> can be combined with laser-induced MXene-derived TiO<sub>2</sub> and 1T-MoS<sub>2</sub>-derived MoO<sub>3</sub> to form various types of asymmetric and symmetric MSCs in the same material system within seconds. The asymmetric MSC exhibits an ultrahigh specific capacitance ( $220 \text{ mF cm}^{-2}$  and  $1101 \text{ F cm}^{-3}$ ), cycling stability (98.3% capacitance retention after 15,000 cycles), energy density ( $0.495 \text{ Wh cm}^{-3}$ ) and power density ( $28 \text{ kW cm}^{-3}$ ). This versatile strategy overcomes the current limitations of MSC manufacturing. Multitype MSCs fabricated herein have high resolution, enhancing the feasibility and flexibility of the preparation of microscale energy storage devices.

## Introduction

The growing demand for miniaturized, multifunctional portable electronics has greatly stimulated the development of microintegrated energy systems. The microsupercapacitor (MSC) plays an integral role in microscale energy storage devices.<sup>[1]</sup> With technological advances, various types of MSCs have been developed. Unlike symmetric MSCs, asymmetric MSCs can be assembled using two electrode materials, providing a larger voltage window and significantly increasing the energy density.<sup>[2, 3]</sup> Thus, the practical applications of MSCs can be extended.

Substantial progress has been made for asymmetric MSCs in recent years. Conventional asymmetric MSCs are referred to as sandwich-type MSCs. Thinner, smaller, more flexible planar asymmetric MSCs require multiple fabrication steps and are difficult to further downsize.<sup>[4, 5]</sup> Specifically, the preparation process is extremely complex because of the unique structure of the inconsistent electrode materials, and accurate control of the electrode materials is challenging. The minimum size of asymmetric supercapacitors remains at the micron or millimeter level. The precise control of electrode material assembly, as well as the simultaneous formation of patterns of two types of materials in one step, is challenging to accomplish through conventional methods such as electrodeposition,<sup>[6]</sup> inkjet printing,<sup>[7]</sup> laser etching,<sup>[8]</sup> and photolithography.<sup>[9]</sup> Pseudocapacitance materials are common asymmetric electrode materials, but due to their instability and poor electrical conductivity, their power density is low and their lifespan is short. In recent years, two-dimensional materials have attracted considerable scholarly attention because of their excellent electrochemical properties. 1T-MoS<sub>2</sub> and MXene, the most notable, have highly reversible surface redox reactions and favorable metallic conductivity.<sup>[10, 11]</sup> A recent study reported that 1T-MoS<sub>2</sub> demonstrated excellent conductivity and a high cycle life as an electrode material for asymmetric supercapacitors. Moreover, the voltage window was large.<sup>[12]</sup> In other investigations,

MXene materials were combined with various metal oxides and carbon-based materials to construct asymmetric supercapacitors, which achieved excellent electrochemical performance.<sup>[13, 14]</sup>

In this study, we present a method for the ultrafast fabrication of submicron-scale symmetric and asymmetric MSCs on the same 1T-MoS<sub>2</sub>/MXene thin films by using temporally and spatially shaped femtosecond laser. Three types of MSCs, namely a 1T-MoS<sub>2</sub>/MXene symmetric MSC, a laser-induced symmetric MSC prepared on MXene-derived TiO<sub>2</sub> and 1T-MoS<sub>2</sub>-derived MoO<sub>3</sub> thin films, and an asymmetric MSC prepared on 1T-MoS<sub>2</sub>/MXene/laser-induced MXene-derived TiO<sub>2</sub> and 1T-MoS<sub>2</sub>-derived MoO<sub>3</sub> thin films, were fabricated. The composition of the laser-induced MoO<sub>3</sub> and TiO<sub>2</sub> thin films was manipulated through laser pulse delay and energy. Using the proposed approach, more than 150 groups of MSCs could be fabricated every minute, and each MSC was only 10 × 10 μm<sup>2</sup> in size. The minimum line width of the MSCs was 200 nm. As expected, the asymmetric MSCs had large voltage windows (1.8 V), excellent specific capacitance (220 mF cm<sup>-2</sup> and 1101 F cm<sup>-3</sup>), and high energy density (0.495 Wh cm<sup>-3</sup>). Notably, the asymmetric MSCs exhibited excellent electrochemical performance across a wide range of scan rates (1–500 V s<sup>-1</sup>), achieving a peak power density of 28 kW cm<sup>-3</sup>. Furthermore, they could be flexibly attached to various substrates, including flexible substrates, and they demonstrated a long cycle life (98.3% capacitance retention after 15,000 cycles) and excellent mechanical flexibility. The present strategy contributes to the miniaturization and practical application of asymmetric MSCs, providing a new direction in the development of multitype microscale energy storage devices in scalable manufacturing.

## Discussion

### The Preparation of Multitype MSCs

First, 1T-MoS<sub>2</sub>/MXene hybrid thin films of variable thickness were prepared through vacuum filtration. We transferred thin films of differing thicknesses to the glass substrate. As shown in Figure 1a, a confocal spatial pulse shaping system for femtosecond lasers was constructed to achieve ultrafast, high-precision patterning. In this process, materials are subjected to laser ablation according to controllable energy. By designing any combination of light fields, various types of symmetric and asymmetric MSCs can be fabricated. Almost any material, including ultrahard, ultrastrong materials, can be subjected to such processing.<sup>[15]</sup> Phase-adjustable spatial light modulators (SLMs) were employed to focus the Gaussian femtosecond laser into a femtosecond laser with a varying spatial distribution. Through the design of distinct phases, arbitrary changes in the light field were realized within an extremely short period to produce multiple types of MSCs. SLMs can load computer-generated holograms (CGHs) to focus light in space. Before the Gaussian laser entered the SLM, it was focused using a Michelson interferometer. The Gaussian femtosecond pulse was integrated into an evenly divided double pulse sequence with a pulse delay of 10 ps. The subsequent subpulses focused the laser on the material in the preceding sequence. When the front sequence pulse contacted the material, numerous freely moving electrons were excited.

The subsequent pulse sequence further interacted with the seed electrons generated by the front sequence pulse before the material was modified or ablated, leading to the avalanche ionization of more free electron eruptions. This occurrence is because the pulse delay between the two pulse sequences is in the picosecond order, which is substantially shorter than the time required for material phase transition.

For our initial beam (800 nm, 35 fs), we customized a special algorithm to calculate the original incident beam, adjusting it according to our target light field. The optimized GS algorithm ensured a more uniform light field distribution.<sup>[16]</sup> In previous experiments using SLM, each pattern corresponded to a CGH.<sup>[17, 18]</sup> However, considering the pattern processing of multiple types of MSCs, various patterns must be processed in the asymmetric MSCs in situ at the same time. Thus, the processing technology requires optimization. We overlaid the target pattern on multiple target images, and programming was applied to load various CGHs into SLMs to realize continuous changes in multiple light fields over a 0.001-s duration. Multiple spatially focused light fields were smoothly focused by the objective lens from the SLM outlet through the 4f relay system. As shown in Figure 1b, we irradiated the original material (1T-MoS<sub>2</sub>/MXene) with different shaped pulse lasers, and used shaped light field 1 to remove the 1T-MoS<sub>2</sub>/MXene, and shaped pulse lasers 2 and 3 to modify the material to obtain laser-induced MXene-derived TiO<sub>2</sub>/1T-MoS<sub>2</sub>-derived MoO<sub>3</sub>. The whole process realizes two processes of laser induced material synthesis and laser removal. As displayed in Figure 1c, when light field pattern 1 was individually focused and processed on the thin film sample, a high-precision symmetric MSC (1T-MoS<sub>2</sub>/MXene) with an adjustable size was fabricated. At this point, ablation was performed by the laser focused using light field pattern 1. By adjusting energy or controlling the number of subpulse repetitions, light field 1 could completely remove the material, whereas light field 2 required laser induction to modify the material. When light field patterns 1 and 2 were combined to focus on the thin film sample, we obtained the same precision size of the asymmetric MSC (1T-MoS<sub>2</sub>/MXene//laser-induced MXene-derived TiO<sub>2</sub>/1T-MoS<sub>2</sub>-derived MoO<sub>3</sub>). The simultaneous projection of light fields 1, 2, and 3 produced two symmetric MSCs (laser-induced MXene-derived TiO<sub>2</sub> and 1T-MoS<sub>2</sub>-derived MoO<sub>3</sub>). As presented in Figure 2a, the patterns of the target light field obtained were different and could be arbitrarily combined to form multiple types of MSCs. The various types of MSCs fabricated had ultrahigh resolution (line width  $\geq 200$  nm), were extremely small ( $10 \times 10 \mu\text{m}^2$ ), had extremely high processing consistency, and could be rapidly prepared in a very short time (150 groups/min) across a large area (Figures 2b and 2c). The MSCs clearly exhibited regularity, and the minimum line width was continuous. The interdigital MSCs with differing shapes and fingers could be completely prepared, such that the influence of fingers on electrochemical performance could be determined. MSCs of different shapes were prepared by controlling the shapes of the target light field (Supplementary Figure 1). This enabled the controllable and personalized preparation of microscale electronics, and the flexibility surpassed that achieved through conventional processing techniques. Moreover, we could control the laser frequency in the actual processing procedure; laser pulses could be shot out of the laser extremely rapidly. In the processing of MSCs with a size of  $10 \times 10 \mu\text{m}^2$ , the translational was set to move at a rate of 2000  $\mu\text{m}/\text{s}$  under a laser frequency of 200. Therefore, 200 subpulses could be used to pattern 200 symmetric MSCs in 1 s. However, because multiple patterned

light fields are required to realize the fabrication of an asymmetric MSC, the maximum number of MSCs processed per second is 100. Supplementary Figure 2 presents MSCs arrays (with varying sizes and line widths) prepared through this method. As indicated in Supplementary Figure 3, we designed patterned MSCs with differing line widths by adjusting the patterns and parameters of the light field with focused laser pulses. These line widths were adjustable from the micron scale (5  $\mu\text{m}$ ) to the nanometer scale (200 nm). Furthermore, we achieved ultrahigh-resolution machining by setting a delay in temporally and spatially shaped femtosecond laser to control pulse shaping near the ablation threshold of the material. We employed femtosecond laser pulses to realize one-step pattern processing of various electrode material systems because this technology can be used to process almost any material.

As shown in Figure 2d, regular pattern processing was conducted on various materials (a metal–organic framework, graphene,  $\text{WS}_2$ ,  $\text{MoTe}$ ,  $\text{MnO}_2$ , and  $\text{RuO}_2$ ). Raman characterization of the laser-patterned area confirmed the complete removal of the material through laser ablation. This demonstrates that our technology can not only be applied to the pattern processing of two-dimensional materials but also be employed for the high-precision processing of metal oxide materials. These results indicate that our technology is promising for the preparation of microelectronics and microscale energy storage devices. We conducted a review of technologies used in the processing of asymmetric supercapacitors. Supplementary Table 1 presents a comparison of our technology with other processes in terms of the size and the maximum resolution of the asymmetric supercapacitors fabricated. Our asymmetric MSCs are at the micron scale, which is dozens or even hundreds of times smaller than conventional asymmetric MSCs. Moreover, our technology greatly enhances the processing resolution of asymmetric MSCs.

## **Characterization and Analysis of Laser-Induced MXene/1T-MoS<sub>2</sub> Materials**

Figure 2e presents scanning electron micrographs of the surface morphology of the composite material before and after processing. The numerous metal oxide particles generated on the material surface after plastic laser processing indicate that oxidation occurred during processing. Supplementary Figure 4 depicts the characterization of the composed material ablated by the focused laser under various parameters. The scanning electron micrographs in Supplementary Figure 3 (a–f) demonstrate that as the laser energy increased, nanoparticles appeared on the surface of the laser-induced material, and the morphology and size of the nanoparticles underwent regular changes as the laser energy changed. These nanoparticles ranged from approximately 10 to 30 nm in size, considerably increasing the specific surface area of the material and providing a greater number of sites for the generation of laser-induced metal oxides. The transmission electron micrographs and selected area electron diffraction patterns of the laser-induced 1T-MoS<sub>2</sub>-derived  $\text{MoO}_3$  and MXene-derived  $\text{TiO}_2$  (MT) thin films ablated by the focused laser under various parameters. The transmission electron micrographs and high-resolution transmission electron micrographs of laser-induced materials (Figure 2f) confirm the presence of  $\text{TiO}_2$  and  $\text{MoO}_3$ . We labeled the composed materials induced by the focused laser at 10 mW with no pulse delay as MT-10/0. Supplementary Figure 4 presents the transmission electron micrographs and selected area electron

diffraction patterns of MXene/1T-MoS<sub>2</sub>, MT-10/0, MT-10/10, MT-20/0, MT-20/10, MT-30/0, and MT-30/10. Lattice fringes are observable in the high-resolution transmission electron micrographs in Supplementary Figure 5, where the d-space of 0.35 nm corresponds to the (101) plane of anatase TiO<sub>2</sub>.<sup>[19]</sup> In the high-resolution transmission electron micrographs of typical orthogonal MoO<sub>3</sub> nanorods, lattice fringes are clearly visible. The distance between adjacent fringes is approximately 0.23 nm, indicating that the nanorods grew in the (200) direction.<sup>[20]</sup> MT was found among laser-induced materials, but the morphology differed due to the influence of laser power and pulse delay. The transmission electron micrographs revealed that the corresponding metal oxides were formed during the laser ablation of MXene/1T-MoS<sub>2</sub>. We speculate that the temporally and spatially shaped femtosecond laser first excited a large number of free electrons. After laser pulse bombardment, these free electrons increased in number. The extremely high instantaneous power of the femtosecond laser pulses generated defects in the Mo–S and Ti–C bonds. The numerous free electrons facilitated the combination of the femtosecond laser pulses with oxygen in the air. Moreover, the femtosecond laser pulses ionized to the oxygen to produce oxygen bonds. Thus, the original MXene material was easily transformed into metal oxide.

To further explore the effect of laser ablation on MXene/1T-MoS<sub>2</sub>, X-ray photoelectron spectroscopy (XPS) was conducted. Studies have reported that the binding energy of 1T-MoS<sub>2</sub> is almost 0.9 eV lower than that of 2H-MoS<sub>2</sub> in non-laser-processed materials.<sup>[19, 21]</sup>

As presented in Figure 3a, the high-resolution XPS spectra of Mo 3d could be deconvoluted into peaks assigned to Mo 3d<sub>3/2</sub> and Mo 3d<sub>5/2</sub>. The peaks at 231.6, 232.8, 234.6, and 235.8 eV in various MT thin films indicated that the Mo 3d<sub>5/2-3/2</sub> doublets corresponded to MoO<sub>3</sub> and MoS<sub>2</sub> (with Mo<sup>5+</sup> 3d<sub>5/2</sub> peaks at 231.6 eV, Mo<sup>5+</sup> 3d<sub>3/2</sub> peaks at 234.6 eV, Mo<sup>6+</sup> 3d<sub>5/2</sub> peaks at 232.8 eV, and Mo<sup>5+</sup> 3d<sub>5/2</sub> peaks at 235.8 eV, respectively).<sup>[19, 24]</sup> The content of Mo in distinct valence states could be summarized from XPS analysis. The Ti2p spectra confirmed the presence of TiO<sub>2</sub>. The peaks centered at 455.1 and 461.2 eV (Figure 3b) corresponded to Ti–C bonds. The peaks centered at 458.5 and 464.4 eV were assigned to Ti–O 2p<sub>3/2</sub> and Ti–O 2p<sub>1/2</sub>, revealing that the oxygen in TiO<sub>2</sub> resulted in the formation of C–Ti–O.<sup>[25, 26]</sup> As shown in Table 1, the proportion of Mo fluctuated with changes in laser power and pulse delay, confirming that the composition of mixed materials and the content of MoO<sub>3</sub> can be adjusted by modifying laser parameters. Results regarding the unprocessed MXene hybrid materials and the TM materials laser processed under various parameters were also summarized. After laser ablation, the Ti–C bond in MXene was substantially reduced. By contrast, the Ti–O bond was considerably increased, indicating the production of titanium oxide. As displayed in Figure 3c, three oxygen components at binding energies of 530.3 eV (Ti–O–Ti), 532.1 eV (Ti–OH), and 531.2 eV (O–Mo) are observable in the O 1s spectra. A detailed summary of these results is provided in Supplementary Table 2. Specifically, information on the presence of molybdenum oxide and titanium oxide in the TM materials is presented.

## Effects of Laser Parameters on Materials and Their Electrochemical Properties

When focused laser pulses are applied to MXene and 1T-MoS<sub>2</sub> composite materials, they not only cause changes in the material properties but also produce new laser-induced metal oxide materials. Controlling these composite materials through laser parameters and determining the optimal parameters are of great research relevance. In this study, as shown in Figure 4a, we analyzed changes in the Mo content in the composite material by adjusting the laser power and pulse delay. As the laser power was increased, the proportion of Mo<sup>5+</sup> and Mo<sup>6+</sup> increased gradually, whereas the Mo<sup>4+</sup> content initially decreased substantially and then remained stable. These results can be explained as follows: As the laser pulses acted on the material, Mo<sup>4+</sup> was oxidized and modified, leading to an increase in the valence state. Taken together with the XPS data, these results suggest that the modified Mo formed a more stable bond with oxygen, generating molybdenum oxide. We also analyzed the mixed materials generated by laser-induced MXene targets. As presented in Figure 4b, the proportion of Ti–C bonds in MXene decreased as the laser power was increased. At the same time, the Ti–O bonds increased gradually. This is in line with the premise that the laser pulses acted on 1T-MoS. In sum, metal oxides were formed during laser processing. When the laser power remained unchanged but the pulse delay was adjusted, a slight change was noted in the composite material. This is mainly related to the ionization of electrons and materials under the pulse delay. An increase in the pulse delay resulted in increased valence states and a more uniform distribution of Mo and Ti in the composite material. This also confirms that the pulse delay excited more electrons, promoting complex chemical reactions such as the redox reactions of Mo and Ti.

The X-ray diffraction patterns of different MT and MXene/1T-MoS<sub>2</sub> were analyzed (Figure 4c). The diffraction peaks of MXene/1T-MoS<sub>2</sub> located at 7.78°, 14.38°, 18.28°, and 28.2° corresponded to the expected diffraction (002) peak of MXene, (002) peak of MoS<sub>2</sub>, (006) peak of MXene, and (004) peak of MoS<sub>2</sub>, respectively.<sup>[25, 27]</sup> When the focused laser pulses were applied to the material, the diffraction peaks changed considerably. The characteristic diffraction peaks of the original MXene/1T-MoS<sub>2</sub> remained. Moreover, many new characteristic diffraction peaks were detected at 12.86°, 25.27°, 26.90°, 38.18°, 54.69°, and 62.47°. They corresponded to the diffraction peaks characteristic of the (020), (040), and (112) crystal planes of MoO<sub>3</sub>, as well as to those of the (101), (004), (204) crystal planes of anatase TiO<sub>2</sub>, confirming the effective oxidation of Ti and Mo layers in MXene/1T-MoS<sub>2</sub> during laser ablation. The differing peak intensities of the characteristic peaks and the slightly stronger intensity of TM10 may be related to the extensive modification of the MXene material under laser pulsing.

To further examine the content of titanium oxide and molybdenum oxide in the composite materials, the Raman spectra of all samples were analyzed (Figure 4d). Obvious peaks at 50–900 cm<sup>-1</sup> corresponding to the distinct vibration modes of the composite materials are observable. Regarding MXene/MoS<sub>2</sub>, the peaks located at 198 and 710 cm<sup>-1</sup> were related to the A<sub>1g</sub> group vibrations of Ti and C atoms. Notably, the additional strong peaks at 167 (J1), 225 (J2), and 387 (J3) cm<sup>-1</sup> were consistent with those of 1T-MoS<sub>2</sub>. Moreover, the other peaks of the E<sub>g</sub> group vibrations of MXene are in line with those reported in other studies.<sup>[27, 28]</sup> Small peaks of molybdenum oxide near 263, 342 and 831 cm<sup>-1</sup> were assigned to the orthorhombic MoO<sub>3</sub> compound.<sup>[29]</sup> These characteristic peaks were located at 150, 198, 401, 515, and

641  $\text{cm}^{-1}$ , confirming the presence of anatase  $\text{TiO}_2$ .<sup>[30]</sup> We conducted electrochemical tests on the MSCs processed under various laser parameters, and the cyclic voltammetry (CV) curves are shown in Figure 4e. The MSCs had excellent electrochemical performance, which may be due to the laser ablation–induced production of multivalent molybdenum oxide in the hybrid materials. The multivalent metal oxides affected the electrochemical performance of the materials. Because of the material modification threshold, the femtosecond laser pulses fully oxidized the material. Moreover, to maximize electrochemical performance, the electrode material on the surface was not removed. Figure 4f demonstrates the influence of laser parameters, including the laser pulse delay, on MSC performance.

## Electrochemical Performance Of The Multitype Mscs

To investigate the contribution of the each component to the electrochemical performance of hybrid electrode materials in the symmetric MSCs. We tested the electrochemical performance of 1T-MoS<sub>2</sub>/MXene and MXene-derived TiO<sub>2</sub>/1T-MoS<sub>2</sub>-derived MoO<sub>3</sub> in a three electrode cell with 1M H<sub>2</sub>SO<sub>4</sub> as aqueous electrolyte (Supplementary Figure 6). And the electrochemical storage mechanism of our hybrid electrode, the electrical double layer capacitance and diffusion-limited capacitance contributions of the total capacitance are performed in Supplementary Figure 7 and 8. The result shows that the proportional capacitance is contributed by capacitive process (electrical double layer or outer surface) and the diffusion-limiting process (inner surface). We tested the electrochemical properties of the various MSCs and compared their differences. Regarding the performance of the symmetric MSCs, Figures 5a and 5b display the CV curves of the MSCs corresponding to the two-material systems (MXene/1T-MoS<sub>2</sub> and MXene-derived TiO<sub>2</sub> and 1T-MoS<sub>2</sub>-derived MoO<sub>3</sub>) in 1M H<sub>2</sub>SO<sub>4</sub> aqueous electrolyte. They all exhibited a rectangular shape, demonstrating that the MSCs processed through this method have favorable capacitance characteristics. As shown in Figure 5c, the MXene/1T-MoS<sub>2</sub> MSCs slightly outperformed the MXene-derived TiO<sub>2</sub>/1T-MoS<sub>2</sub>-derived MoO<sub>3</sub> MSCs. This is mainly attributable to the excellent conductivity and capacitance properties of two-dimensional materials; the conductivity of metal oxides is slightly inadequate in comparison. The galvanostatic charge–discharge (GCD) profiles of the two types of MSCs (Figures 5d and 5e) are consistent with previous results. A performance comparison of the two MSCs with differing electrode materials was conducted on the basis of the CGD profiles. To clearly observe the differences in performance, we compared the CV curves generated at the same scan rate and the GCD profiles established at the same current density (Figures 5g–5i).

Next, the asymmetric MSCs were subjected to comprehensive electrochemical testing. As shown in Figure 6a, favorable capacitance characteristics were retained even after the voltage window was expanded from 1.2 to 1.8 V in 1M H<sub>2</sub>SO<sub>4</sub> aqueous electrolyte. This large voltage window contributed to the high energy density of the asymmetric MSCs. Through our approach, the shapes, number of fingers, and microscopic size of the interdigitated MSCs were controlled. As presented in Figure 2, interdigitated MSCs with various numbers of fingers were fabricated, and the influence of the number of fingers on electrochemical performance was investigated. Curves in GCD profiles generated under the same current density of 1.8 V indicated favorable characteristics. The GCD profiles in Figure 6b indicated that MSCs

with more fingers outperformed those with fewer fingers; this is related to the area of the active interface site in contact with the electrolyte. Multiple fingers can increase electrode–electrolyte contact and facilitate rapid charge transfer, thus enhancing electrochemical performance. CV curves were measured according to the change in scan rates. A rectangular shape and similar curves were noted (Figure 6c). The specific capacitance results support that MSCs with more indexes have more favorable electrochemical performance. We examined the electrochemical properties of MSCs with four fingers. Figures 6d and 6e display the GCD profiles and CV curves corresponding to these MSCs under various current densities and scan rates, respectively. We determined the areal and volumetric capacitance of the MXene-derived  $\text{TiO}_2/1\text{T-MoS}_2$ -derived  $\text{MoO}_3/\text{MXene}/1\text{T-MoS}_2$  MSCs under changes in scan rate ( $220 \text{ mF cm}^{-2}$  and  $1101 \text{ F cm}^{-3}$ , respectively). Notably, our MSCs had ultrahigh electrochemical performance even under an extremely high scan rate of  $50 \text{ V s}^{-1}$ ; in other words, our MSCs have favorable rate performance (Supplementary Figure 9). Nyquist plots of the multitype MSCs (Figure 6g) show slopes approaching  $90^\circ$  in the high frequency range, indicating that the MSCs have excellent capacitance characteristics and are potentially applicable to various material systems. The MXene and  $1\text{T-MoS}_2$  MSCs had the lowest equivalent series resistance of  $0.55 \text{ m } \Omega \text{ cm}^{-2}$ . This value is extremely low in the field of MSCs, demonstrating that the internal resistance of the MSCs is extremely low. No semicircles were detected, indicating the absence of charge transfer resistance. Furthermore, the vertical straight line at the low frequency in the Nyquist plot confirms the rapid diffusion of ions to electrodes and the presence of electron transfer. The MXene-derived  $\text{TiO}_2/1\text{T-MoS}_2$ -derived  $\text{MoO}_3/\text{MXene}/1\text{T-MoS}_2$  MSCs exhibit a long cycle life and favorable cycling stability (Figure 6h). Notably, the MSCs retained more than 98.8% of the initial capacitance after 15,000 cycles. For comparison, we extracted several GCD profiles from the loop. They were almost consistent under a voltage window of 1.8 V. CV curves of asymmetric MSCs under differing bending states were generated (Supplementary Figure 10). The CV curves were generally consistent, indicating that the MSCs had excellent flexibility and flexural resistance. Figure 6i presents a Ragone plot comparing the energy and power density of our MSCs and other energy storage devices.<sup>[16, 31–34]</sup> The energy density of  $0.495 \text{ Wh cm}^{-3}$  achieved in the present study is several orders of magnitude higher than those of other capacitors or batteries. It is also substantially higher than those of MSCs presented in previous studies. In addition, our MSCs exhibited an excellent power density of  $28295 \text{ W cm}^{-3}$ , which is attributable to its favorable capacitance characteristics under a high scan rate. In sum, our MSCs have high potential for application to microscale energy storage devices.

## Conclusion

Through our simple maskless patterning approach, high-performance multitype MSCs were prepared. Leveraging the unique advantages of temporally and spatially shaped femtosecond laser, the ultrafast fabrication of multipatterned MSCs was realized. Our method can be applied to various material systems, including to the construction of asymmetric electrode structures from laser oxidation materials. The MXene-derived  $\text{TiO}_2/1\text{T-MoS}_2$ -derived  $\text{MoO}_3/\text{MXene}/1\text{T-MoS}_2$  MSCs exhibited ultrahigh specific capacitance ( $220 \text{ mF cm}^{-2}$  and  $1101 \text{ F cm}^{-3}$ ), cycling stability (98.3% capacitance retention after 15,000

cycles), energy density ( $0.495 \text{ Wh cm}^{-3}$ ), and power density ( $28 \text{ kW cm}^{-3}$ ). Our new micromachining and packaging technologies [CC1] are expected to promote the application of MSCs in the field of system-on-chip technology[CC2]. Flexible, stretchable planar MSCs can be integrated into artificial skin, wearable electronics, and even brain-computer interfaces[CC3]. In some cases, MSCs can replace batteries or serve as an energy solution when high cycling stability[CC4], long cycle life, and a fast power supply are required.

This is the first specific mention of micromachining and packaging in this paper. Are you referring to the proposed ultrafast fabrication method? Please review.

This appears to better reflect your intended meaning. Please review.

This is the idiomatic term. Please review.

The meaning of “large cycles” is unclear. Please review this change.

## Methods

### MXene/1T-MoS<sub>2</sub> thin film Preparation

MXene dispersion ( $2.5 \text{ mg mL}^{-1}$ , 200-500 nm) purchased from Nanjing/Jiangsu XFNANO Materials Tech Co., Ltd was mixed with the suspended chemically exfoliated single-layer 1T-MoS<sub>2</sub> nanosheets dispersion purchased from Nanjing/Jiangsu XFNANO Materials Tech Co., Ltd. The two solutions underwent exfoliation for 5h, separately. Then, the two diluted mixed solutions were mixed together, treated by sonication for 2 h and stirred for 1 h. The prepared mixed solution was vacuum filtered by fiber filter. About 6 h of filtration, a layer of mixed film was produced, then it was vacuum-dried. Nitrocellulose membrane for vacuum filtration was purchased from Merck Millipore LTD. Sulfuric acid (95%-98%) was obtained from Sigma Aldrich and used to dissolve the cellulose film when transferring the mixed film. In a simple vacuum filtration process, MXene and monolayer MoS<sub>2</sub> nanosheets are filtered through a membrane with an aperture of 25 nm to form a stacked MXene/metal 1T-MoS<sub>2</sub> membrane. The thickness of this re-stacked film is controllable, depending on the volume of the filtered solution. In our test, the thickness of the composite film prepared by us is  $1 \mu\text{m}$ .

### The Shaped femtosecond laser

A Titanium sapphire laser regeneration amplification system was used to transmit a Gaussian beam with a central wavelength of 800 nm and a pulse duration of 35 fs. Holoeye Pluto (spatial light modulator) can receive the phase difference distribution of the load and reflect the beam away. The designed electrode shape determines the intensity distribution by locating a  $256 \times 256$  pixel region to a black  $1080 \times 1920$  background image. We use an improved Gaussian algorithm to optimize the algorithm by increasing the number of iterations and using a function to optimize the distance between the beam spots. So we can get different expected light fields. Then, the gray phase hologram is loaded onto SLM to transform the light field of any geometry. The shape beam is focused by an Olympus objective lens ( $20\times$ ,  $\text{NA} = 0.45$ ). The sample was placed horizontally on the six-axes translation stage (M840.5DG, PI, Inc.).

## Characterization of laser-induced MXene/1T-MoS<sub>2</sub>

The morphology and microstructures were characterized by scanning electron microscope (SEM) using SU8220 (Hitachi, Japan) by a Hitachi SEM in Tsinghua university. X-ray photoelectron spectroscopy (XPS) analysis was performed using a ESCALAB 250Xi spectrometer with a monochromatic Al K $\alpha$  source (7.5  $\mu$ m beam spot). Raman spectra were acquired using a Via-reflex spectroscopy with the excitation laser line at 532 nm. The XRD patterns were conducted on a D8 Advance (Bruker) with CuK $\alpha$  radiation. Using an Olympus metallographic microscope can take optical microscopy images. The Confocal Laser Scanning Microscopy used an MPLAPONLEXT x20 lens. The Raman spectroscopy investigations were performed using a Renishaw inVia Reflex spectrometer with laser wavelength of 532 nm.

## Electrochemical characterization of the result micro-supercapacitors

Further analysis was performed to determine the current density using the software package NanoScope Analysis. Electrochemical testing was performed on a CHI760E electrochemical workstation connected through a Probe Station with polyamide-coated platinum probes (tip diameter, approximately 5  $\mu$ m) as the current collectors. To ensure a stable electrochemistry environment, the open-circuit potential (E<sub>ocp</sub>) measurements were tested for one hour until the fluctuation was of less than 10 mV in 10 minutes before every electrochemistry measurements. The electrochemical performance of the MSCs was measured in a two-electrode system, and analysed according to the cyclic voltammetry (CV), galvanostatic charge/discharge (GCD) and electrochemical impedance spectra (EIS). The areal capacitance (mF cm<sup>-2</sup>) per electrode was derived from the CV and GCD tests by using Eqs. (1) and (2), respectively, as follows:

$$C = \frac{1}{\mathcal{I} \times V} \int_{V_i}^{V_f} I(V) dV \quad (1)$$

where  $I$ ,  $\mathcal{I}$  and  $V$  represent the current applied, scanning rate and voltage ( $V_f$  and  $V_i$  are the final voltage and initial voltage).

$$C = \frac{I}{(-dV/dt)} \quad (2)$$

where  $I$  is the discharge current, and  $dV/dt$  is the slope of the discharge curve. Cycling stability measurements were performed by repeating constant current charge–discharge at 1 mA for 12,000 cycles. The energy densities (mWh cm<sup>-2</sup>) of the supercapacitors were calculated according to the following equations:

$$E_{cell} = C_{cell} \Delta E^2 / (2 \times 3,600) \quad (3)$$

where  $\Delta E$  represents the operating voltage window. Therefore, the power density ( $\mu$ Wh cm<sup>-2</sup>) of the obtained supercapacitor was obtained as follows:

$$P_{cell} = E_{cell} \times 3,600 / t$$

(4)

where  $t$  represents the discharge time ( $t = \Delta V / \vartheta$ ).

## Declarations

### Data availability

All relevant data that support the plots within this article and other findings of this study are available from the corresponding authors upon request.

### Acknowledgements

This research was supported by the Outstanding Youth Science Foundation of China (Grant No. 51922005), the National Natural Science Foundation of China (NSFC) (Grant No. 51775047) and National Natural Science Foundation of China (NSFC) (grants 52105427).

### Author contributions

Y.J. Yuan, L. Jiang and X.Li proposed the research and designed the experiment; The experiments on materials preparation and characterizations of morphology and composition were performed by Y.J. Yuan with the assistance of P. Zuo, L. Ma, C.Y. Chen; Preparation of experimental instruments and construction of optical path performed by Y.J. Yuan with the assistance of M.S. Liang, J.R. Wu, and J.Q. Huang; Y.J. Yuan performed all electrochemical characterization and other experiments. All authors participated in discussion and analysis of results, and the manuscript was collaboratively written by Y.J. Yuan, L. Jiang, L.T. Qu, , X. Li, and Y. Zhao cooperatively. L. Jiang and X. Li provided support and supervision for the project.

### Competing interests

The authors declare no competing interests.

### Additional information

Correspondence and requests for materials should be addressed to Xin Li.

# References

1. M. Salanne, B. Rotenberg, K. Naoi, K. Kaneko, P. L. Taberna, C. P. Grey, B. Dunn, Efficient storage mechanisms for building better supercapacitors. *Nat. Energy***1**, 1-10 (2016).
2. Y. Shao, M. F. El-Kady, J. Sun, Y. Li, Q. Zhang, M. Zhu, B. Dunn, R. B. Kaner, Design and mechanisms of asymmetric supercapacitors. *Chem. Rev.***118**, 9233-9280 (2018).
3. M. Ghidui, M. R. Lukatskaya, M. Q. Zhao, Y. Gogotsi, M. W. Barsoum, Conductive two-dimensional titanium carbide 'clay' with high volumetric capacitance *Nature***516**, 78-81 (2014).
4. A. Yu, I. Roes, A. Davies, Z. Chen, Ultrathin, transparent, and flexible graphene films for supercapacitor application. *Appl. Phys. Lett.* **96**, 253105 (2010).
5. J. J. Yoo, K. Balakrishnan, J. Huang, V. Meunier, B. G. Sumpter, A. Srivastava, M. Conway, A. L. Reddy, J. Yu, R. Vajtai, P. M. Ajayan, Ultrathin planar graphene supercapacitors. *Nano letters* **11**, 1423-1427 (2011).
6. B. Asbani, K. Robert, P. Roussel, T. Brousse, C. Lethien, Asymmetric micro-supercapacitors based on electrodeposited RuO<sub>2</sub> and sputtered VN films. *Energy Storage Mater.***37**, 207-214 (2021).
7. C. J. Zhang, L. McKeon, M. P. Kremer, S. H. Park, O. Ronan, A. Seral-Ascaso, S. Barwich, C. Ó. Coileáin, C. McEvoy, H. C. Nerl, B. Anasori, J. N. Coleman, Y. Gogotsi, V. Nicolosi, Additive-free MXene inks and direct printing of micro-supercapacitors. *Nat. Commun.***10**, 1-9 (2019).
8. L. Zhang, G. Yang, Z. Chen, D. Liu, J. Wang, Y. Qian, C. Chen, Y. Liu, L. Wang, J. R. Razal, W. Lei, MXene coupled with molybdenum dioxide nanoparticles as 2D-0D pseudocapacitive electrode for high performance flexible asymmetric micro-supercapacitors. *J. Materiomics* **6**, 138-144 (2020).
9. S. C. Lee, U. M. Patil, S. J. Kim, S. Ahn, S. W. Kang, S. C. Jun, All-solid-state flexible asymmetric micro supercapacitors based on cobalt hydroxide and reduced graphene oxide electrodes. *RSC Adv.***6**, 43844-43854 (2016).
10. M. R. Lukatskaya, S. Kota, Z. Lin, M. Q. Zhao, N. Shpigel, M. D. Levi, J. Halim, P. L. Taberna, M. W. Barsoum, Y. Simon, Y. Gogotsi, Ultra-high-rate pseudocapacitive energy storage in two-dimensional transition metal carbides. *Nat. Energy***2**, 1-6 (2017).
11. B. Anasori, M. R. Lukatskaya, Y. Gogotsi, 'Lukatskaya, and Y. Gogotsi'. *Nat. Rev. Mater***2**, 1-17 (2017).
12. Y. Shao, J. H. Fu, Z. Cao, K. Song, R. Sun, Y. Wan, A. Shamin, L. Cavallo, Y. Han, R. B. Kaner, V. C. Tung, 3D Crumpled Ultrathin 1T MoS<sub>2</sub> for Inkjet Printing of Mg-Ion Asymmetric Micro-supercapacitors. *ACS Nano***14**, 7308-7318 (2020).
13. Q. Jiang, N. Kurra, M. Alhabeab, Y. Gogotsi, H. N. Alshareef, All Pseudocapacitive MXene-RuO<sub>2</sub> Asymmetric Supercapacitors. *Adv. Energy Mater.***8**, 1703043 (2018).
14. C. Couly, M. Alhabeab, K. L. Van Aken, N. Kurra, L. Gomes, Navarro-Suárez, A. M., Anasori, B., Alshareef, H. N., Gogotsi, Y. Asymmetric flexible MXene-reduced graphene oxide micro-supercapacitor. *Adv. Electronic Mater.***4**, 1700339 (2018).
15. L. Jiang, A. D. Wang, B. Li, T. H. Cui, Y. F. Lu, Electrons dynamics control by shaping femtosecond laser pulses in micro/nanofabrication: modeling, method, measurement and application. *Light-Sci.*

- Appl.* **7**, 17134-17134 (2018).
16. Y. Yuan, L. Jiang, X. Li, P. Zuo, C. Xu, M. Tian, X. Zhang, S. Wang, B. Lu, C. Shao, B. Zhao, J. Zhang, L. Qu, T. Cui, Laser photonic-reduction stamping for graphene-based micro-supercapacitors ultrafast fabrication. *Nat. Commun.* **11**, 1-11 (2020).
  17. R. W. Gerchberg, A practical algorithm for the determination of phase from image and diffraction plane pictures. *Optik* 1972, **35**, 237-246.
  18. R. Di Leonardo, F. Ianni, G. Ruocco, Computer generation of optimal holograms for optical trap arrays. *Opt. Express* **15**, 1913-1922 (2007).
  19. J. Zhou, M. Guo, L. Wang, Y. Ding, Z. Zhang, Y. Tang, C. Liu, S. Luo, 1T-MoS<sub>2</sub> nanosheets confined among TiO<sub>2</sub> nanotube arrays for high performance supercapacitor. *Chem. Eng. J.* **366**, 163-171 (2019).
  20. S. Bai, W. Jiang, Z. Li, Y. Xiong, Structural and electrochemical characterization of MoO<sub>3</sub> nanorod-based electrochemical energy storage devices. *ChemNanoMat* **1**, 223-239 (2015).
  21. M. Acerce, D. Voiry, M. Chhowalla, Metallic 1T phase MoS<sub>2</sub> nanosheets as supercapacitor electrode materials. *Nat. nanotechnol.* 2015, **10**, 313-318.
  22. G. Eda, H. Yamaguchi, D. Voiry, T. Fujita, M. Chen, M. Chhowalla, Photoluminescence from Chemically Exfoliated MoS<sub>2</sub>. *Nano letters* **11**, 5111-5116 (2011).
  23. S. Bai, W. Jiang, Z. Li, Y. Xiong, 1T-MoS<sub>2</sub> nanosheets confined among TiO<sub>2</sub> nanotube arrays for high performance supercapacitor. *ChemNanoMat* **1**, 223-239 (2015).
  24. J. K. Wuenschell, A. B. Payton, J. R. Lince, H. Helvajian, Structural and electrochemical characterization of -MoO<sub>3</sub> nanorod-based electrochemical energy storage devices. *J. Appl. Phys.* **127**, 145305 (2020).
  25. Q. Liu, L. Ai, J. Jiang, Laser processing of thin film sputtered MoS<sub>2</sub>: Thinning, oxidation, and crystallization. *J Mater. Chem. A* **6**, 4102-4110 (2018).
  26. L. Hu, K. Huo, R. Chen, B. Gao, J. Fu, P. K. Chu, Recyclable and High-Sensitivity Electrochemical Biosensing Platform Composed of Carbon-Doped TiO<sub>2</sub> Nanotube Arrays. *Anal. Chem.* **83**, 8138-8144 (2011).
  27. Q. Liu, X. Li, Q. He, A. Khalil, D. Liu, T. Xiang, X. Wu, L. Song, Gram-Scale Aqueous Synthesis of Stable Few-Layered 1T-MoS<sub>2</sub>: Applications for Visible-Light-Driven Photocatalytic Hydrogen Evolution. *Small* **11**, 5556-5564 (2015).
  28. K. Lee, H. Lee, Y. Shin, Y. Yoon, D. Kim, H. Lee, Recent Advances in Functional Thermoelectric Materials for Printed Electronics. *Nano Energy* **26**, 746-754 (2016).
  29. M. M. Alsaif, M. R. Field, B. J. Murdoch, T. Daeneke, K. Latham, A. F. Chrimes, A. S. Zoofaker, S. P. Russo, J. Z. Ou, K. Kalantar-Zadeh, Substoichiometric two-dimensional molybdenum oxide flakes: a plasmonic gas sensing platform. *Nanoscale* **6**, 12780-12791 (2014).

30. J. Zhang, M. Li, Z. Feng, J. Chen, C. Li, UV Raman Spectroscopic Study on  $\text{TiO}_2$ . I. Phase Transformation at the Surface and in the Bulk. *J. Phy. Chem. B***110**, 927-935 (2006).
31. J. C. Li, J. Gong, X. Zhang, L. Lu, F. Liu, Z. Dai, Q. Wang, X. Hong, H. Pang, M. Han, Alternate integration of vertically oriented  $\text{CuSe@FeOOH}$  and  $\text{CuSe@MnOOH}$  hybrid nanosheets frameworks for flexible in-plane asymmetric micro-supercapacitors. *ACS Appl. Energ. Mater.***3**, 3692-3703 (2020).
32. Y. Xie, H. Zhang, H. Huang, Z. Wang, Z. Xu, H. Zhao, Y. Wang, N. Chen, W. Yang, W. Yang, Laser crystallized sandwich-like MXene/ $\text{Fe}_3\text{O}_4$ /MXene thin film electrodes for flexible supercapacitors. *Nano Energy* **74**, 104928 (2020).
33. X. Wang, J. Sun, J. Zhao, Z. Zhou, Q. Zhang, C. P. Wong, Y. Yao, All-solid-state fiber-shaped asymmetric supercapacitors with ultrahigh energy density based on porous vanadium nitride nanowires and ultrathin  $\text{Ni(OH)}_2$  nanosheet wrapped  $\text{NiCo}_2\text{O}_4$  nanowires arrays electrode. *J. Phys. Chem. C***123**, 985-993 (2018).
34. W. Ma, S. Chen, S. Yang, W. Chen, W. Weng, Y. Cheng, M. Zhu, Flexible all-solid-state asymmetric supercapacitor based on transition metal oxide nanorods/reduced graphene oxide hybrid fibers with high energy density. *Carbon***113**, 151-158 (2017).

## Table

Table 1 is available in the supplementary files section.

## Figures

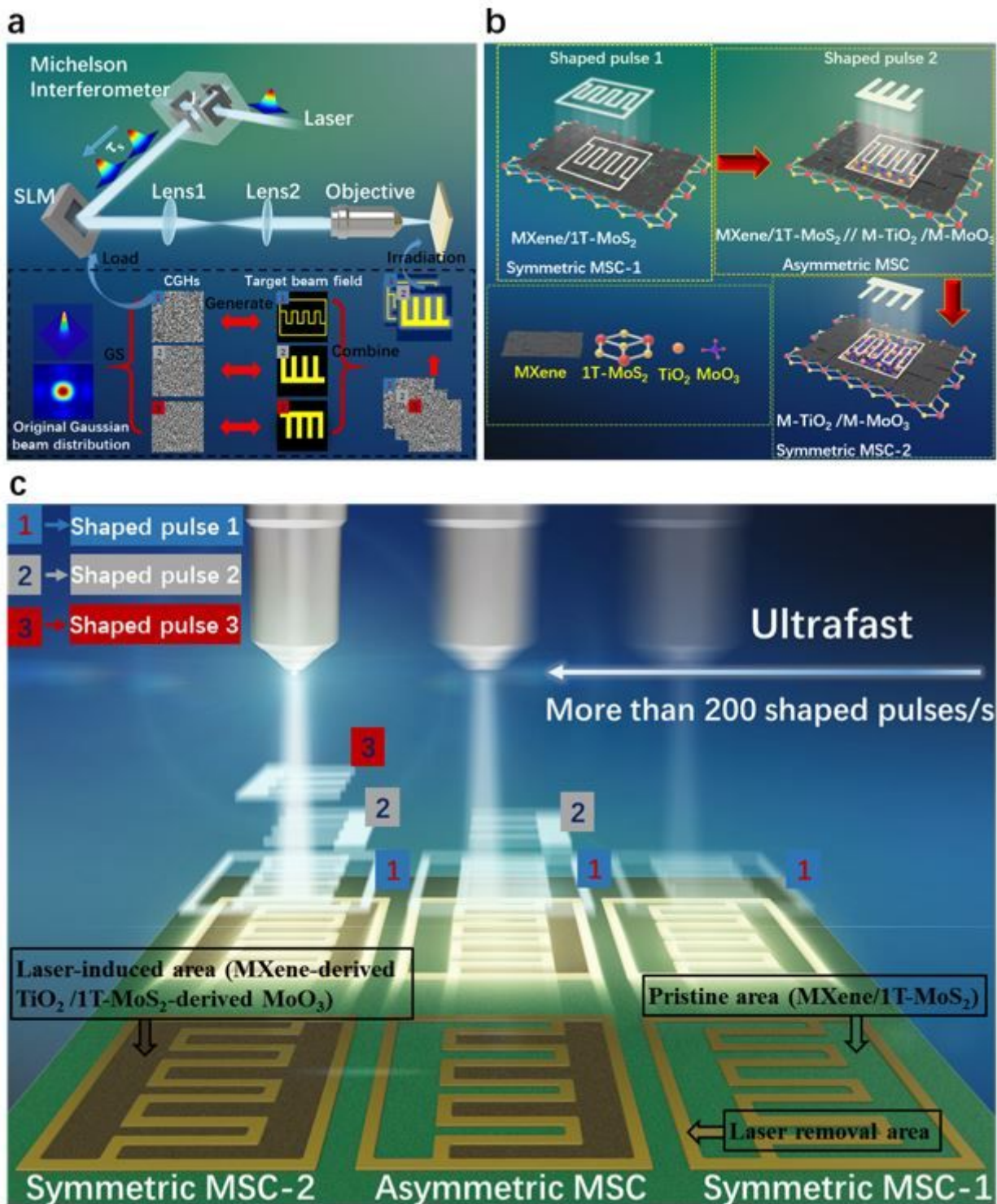
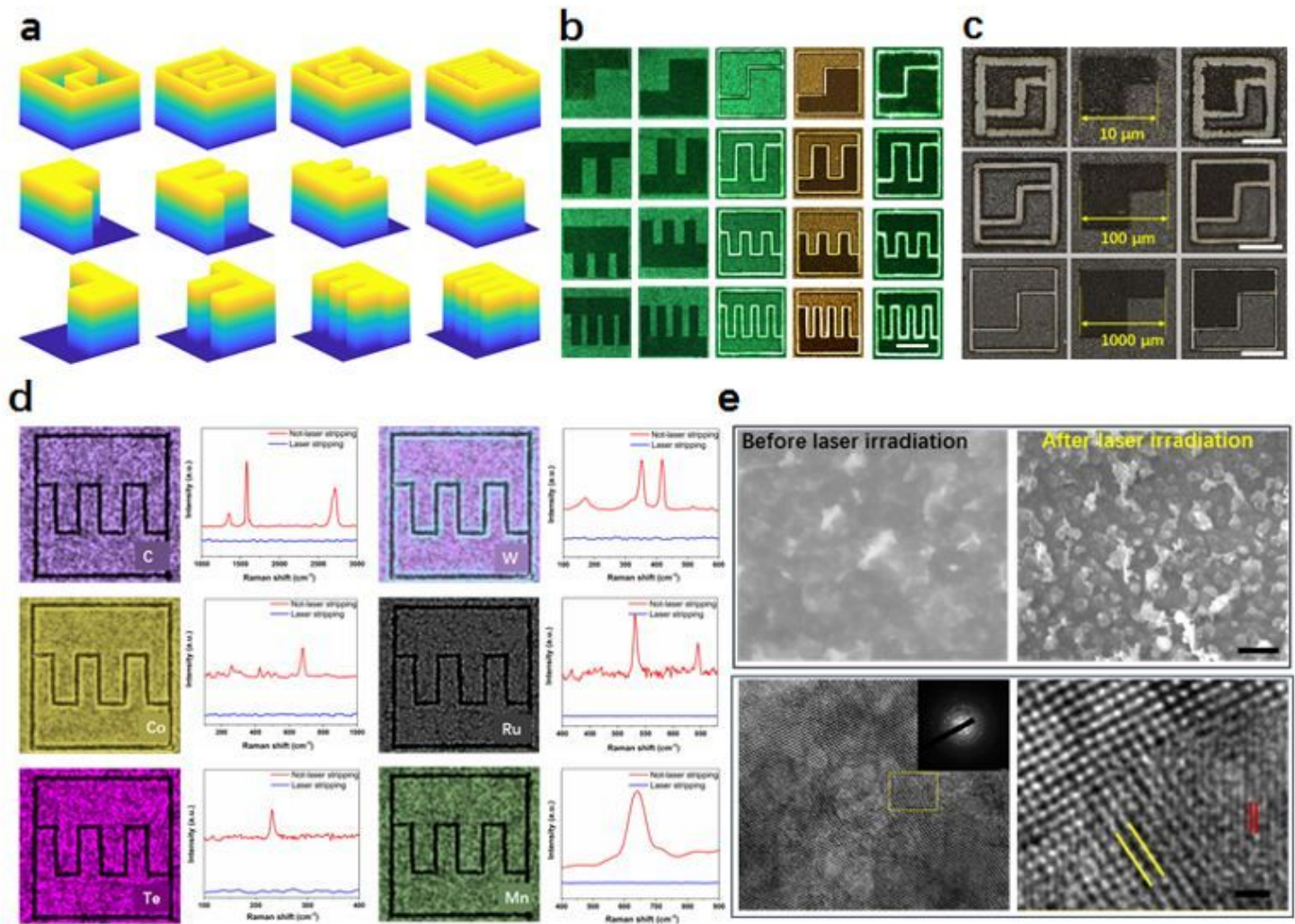


Figure 1

Schematic of the SLM-based maskless patterning method for the ultrafast manufacturing of multitype MSCs. a) The original Gaussian laser is transformed by the Michelson interferometer into a double pulse with a pulse delay. It then passes through the SLM and is transported to the objective lens by the 4f system to realize micro/nano processing. b) The Schematic of the laser-induced synthesis of materials for different MSCs. c) The magnified image of the objective lens and the processed sample can be

processed within an extremely short period of time by controlling the 1, 2, and 3 subpulses to obtain various types of MSCs.



**Figure 2**

a) Light field patterns of differing shapes. b) Optical micrographs of various types of MSCs obtained through processing (scale bars: 10 μm). c) Scanning electron micrographs of MSCs of different sizes. d) Scanning electron microscopy mapping of patterns on different materials and the corresponding Raman spectra. e) Scanning electron micrographs of the material surfaces before and after laser ablation (scale bars: 1 μm). f) Transmission electron micrographs captured after the laser-induced modification of the material (scale bars: 1 nm).

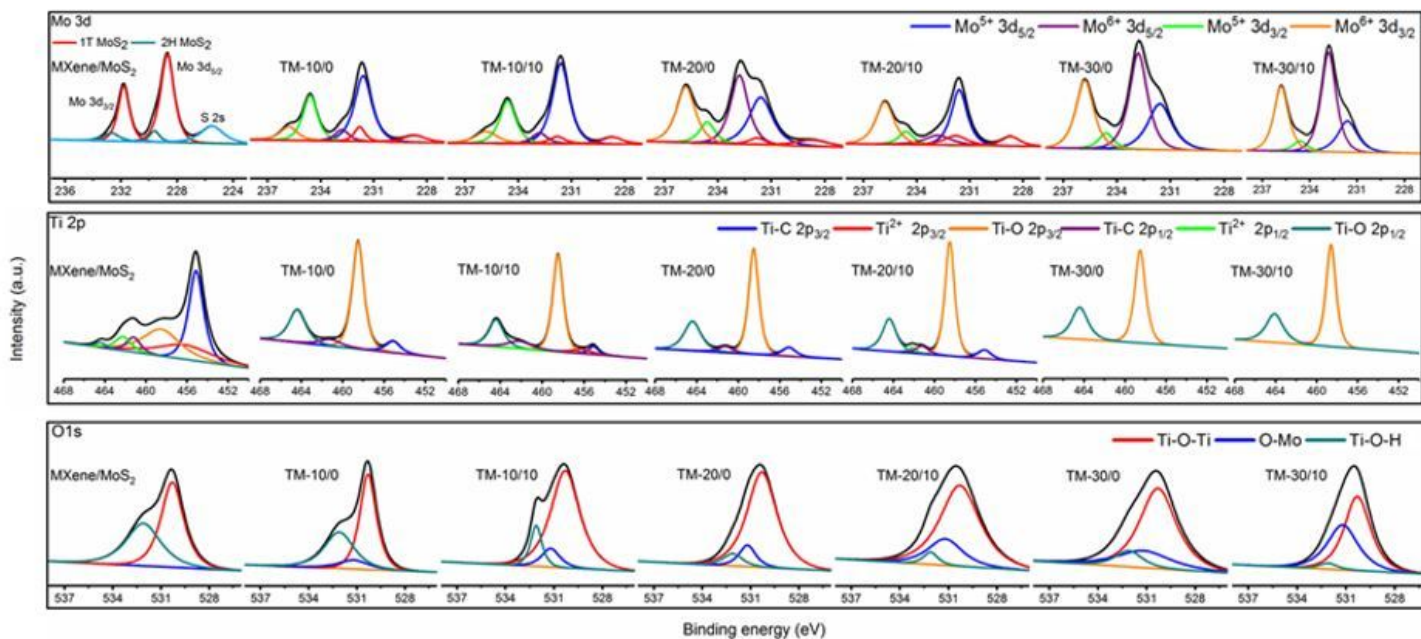
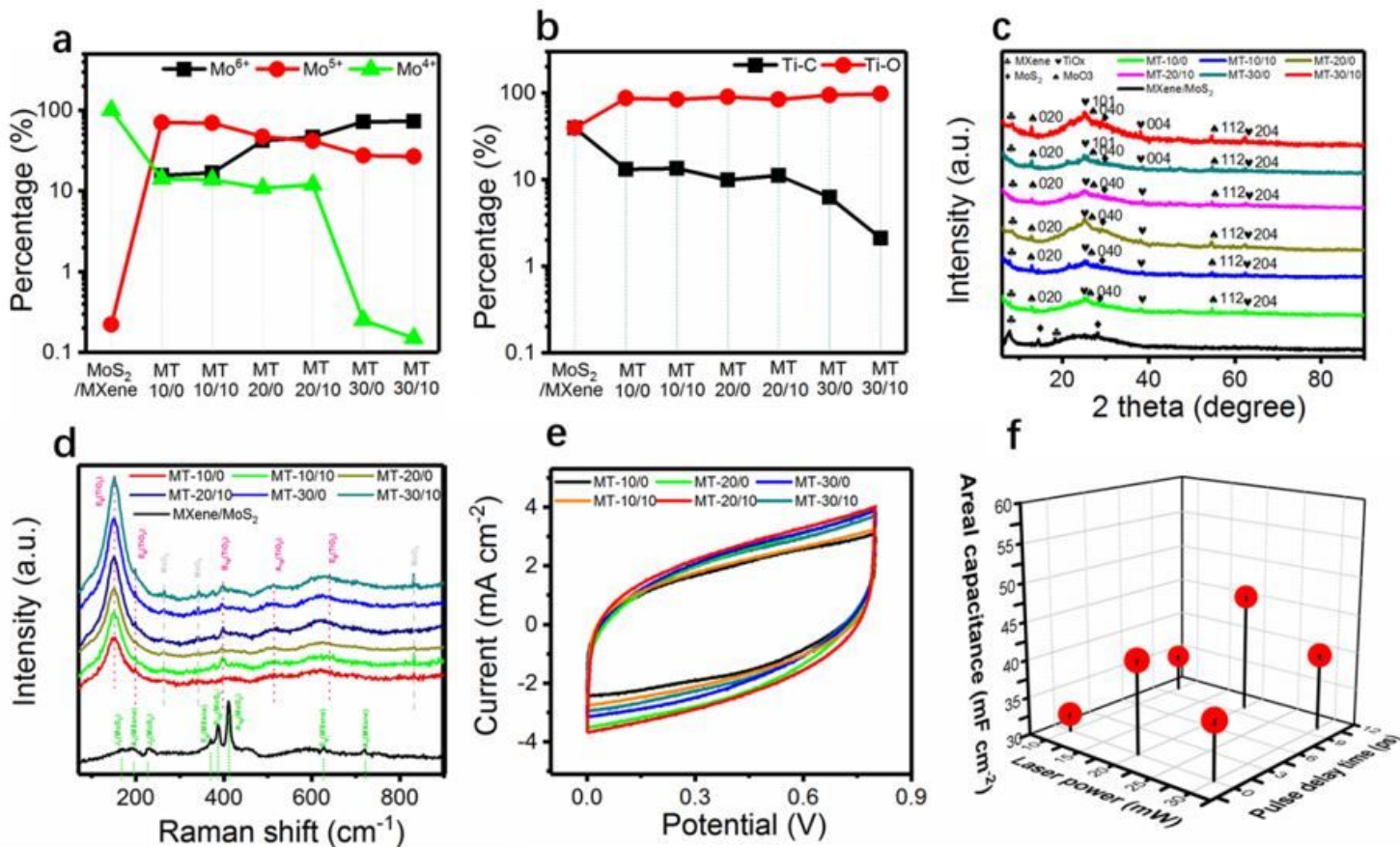


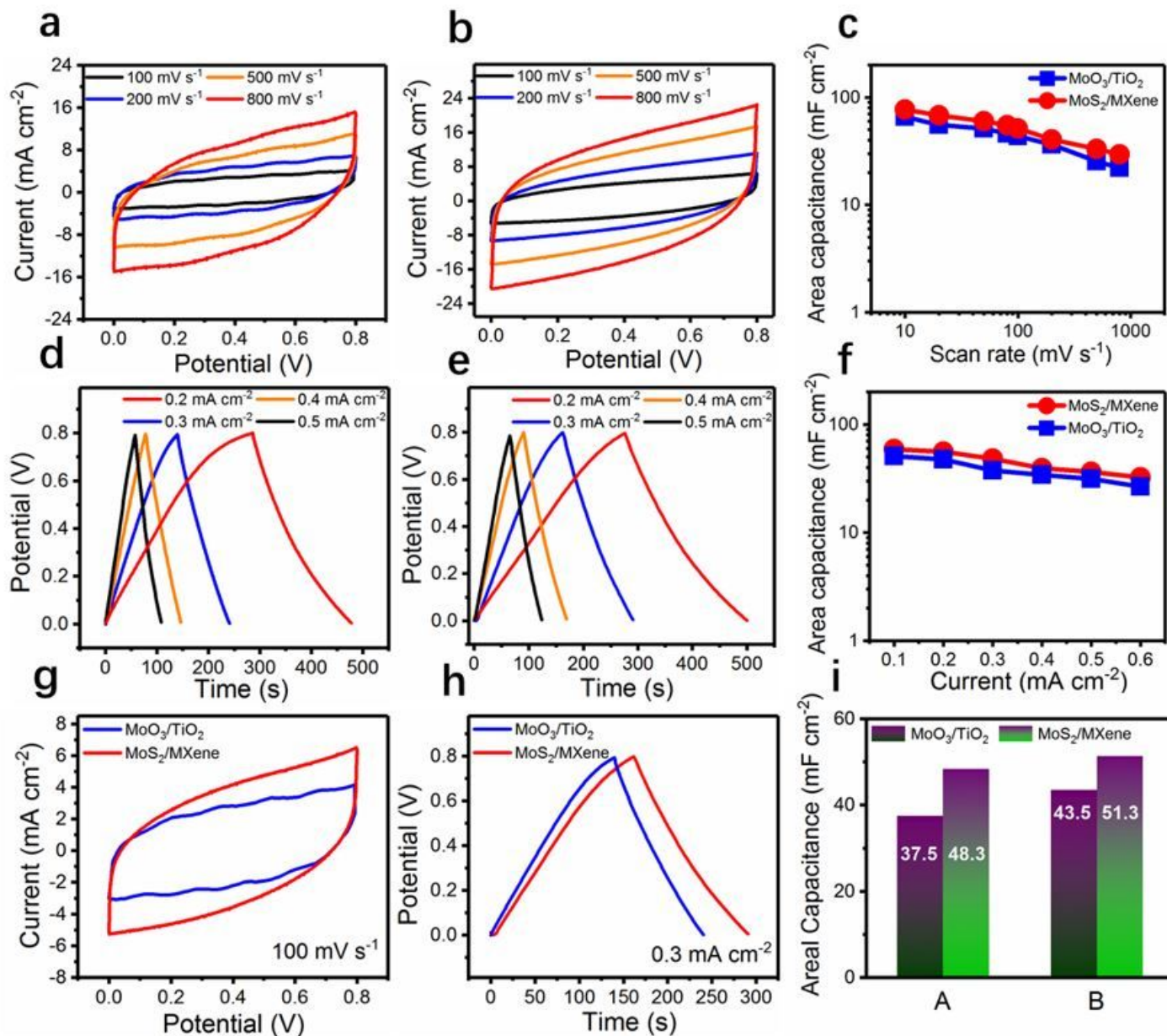
Figure 3

a)–c) Mo 3d, Ti2p, and O 1s peaks observed in the XPS analysis of composites prepared under various laser energy and laser pulse delay conditions.



**Figure 4**

a) Changes in the band content of various valence states of Mo in each composite material. b) Ratio of Ti–C and Ti–O bonds in the synthesized materials under various conditions. c) X-ray diffraction patterns of each composite material. d) Raman spectra of each composite materials. e) cyclic voltammetry curves of the MSCs corresponding to each material. f) Comparison of the performance of MSCs corresponding to various materials.

**Figure 5**

a) and b) Cyclic voltammetry (CV) curves of the two symmetric MSCs under differing scan rates. c) Comparison of the two MSCs' electrochemical performance, as calculated from the CV curves. d) and e) GCD profiles of the two types of MSCs under differing current densities. f) Comparison of the

electrochemical performance of the two MSCs, as determined from the GCD profiles. g) CV curves of the two MSCs under the same scan rate. h) GCD profiles of the two MSCs under the same current density. i) Chart comparing the electrochemical performance of the two MSCs under the same situations.

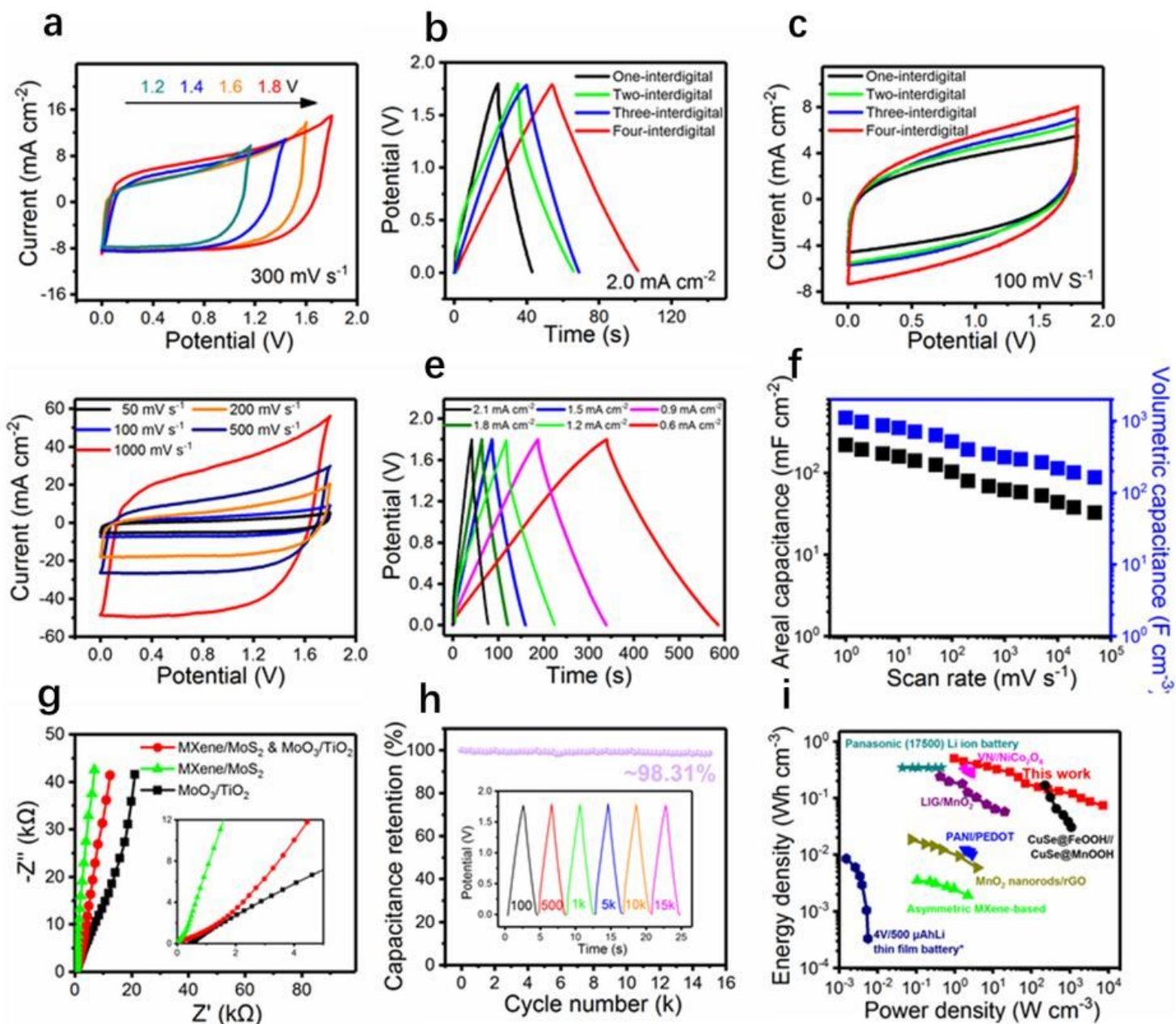


**Figure 6**

a) Cyclic voltammetry (CV) curves of the asymmetric MSCs in a gradually increasing voltage window. b) GCD profiles of the asymmetric MSCs with different fingers in the 1.8-V voltage window. c) CV curves of the asymmetric MSCs with different fingers at a  $100 \text{ mV s}^{-1}$  scan rate. d) CV curves of the asymmetric MSCs under differing scan rates. e) GCD profiles of the asymmetric MSCs under differing current densities. f) Summary of the electrochemical performance of the MSCs under differing scan rates. g) Nyquist plots of the different types of MSCs. h) Cycle life of the asymmetric MSCs (the independent GCD

profiles in the illustration). i) Ragone plot comparing the asymmetric MSCs with other MSCs and microscale energy storage devices.

## Supplementary Files

This is a list of supplementary files associated with this preprint. Click to download.

- [Supplementarymaterial.docx](#)
- [table1.jpg](#)